Higher-order Laguerre-Gauss interferometry for gravitational-wave detectors with *in situ* mirror defects compensation

A. Allocca,[1,2,*] A. Gatto,[3] M. Tacca,[3] R. A. Day,[4] M. Barsuglia,[3] G. Pillant,[4] C. Buy,[3] and G. Vajente[5]

[1]*INFN, Sezione di Pisa, I-56127 Pisa, Italy*
[2]*Università di Siena, I-53100 Siena, Italy*
[3]*APC, AstroParticule et Cosmologie, Université Paris Diderot, CNRS/IN2P3, CEA/Irfu, Observatoire de Paris, Sorbonne Paris Cité, F-75205 Paris Cedex 13, France*
[4]*European Gravitational Observatory (EGO), I-56021 Cascina, Pisa, Italy*
[5]*California Institute of Technology, Pasadena, California 91125, USA*

(Received 5 October 2015; published 18 November 2015)

The use of higher-order Laguerre-Gauss modes has been proposed to decrease the influence of thermal noise in future generation gravitational-wave interferometric detectors. The main obstacle for their implementation is the degeneracy of modes with same order, which highly increases the requirements on the mirror defects, beyond the state-of-the-art polishing and coating techniques. In order to increase the mirror surface quality, it is also possible to act *in situ*, using a thermal source, sent on the mirrors after a proper shaping. In this paper we present the results obtained on a tabletop Fabry-Pérot Michelson interferometer illuminated with a $LG_{3,3}$ mode. We show how an incoherent light source can reduce the astigmatism of one of the mirrors, increasing the quality of the beam in one of the Fabry-Pérot cavities and then the contrast of the interferometer. The system has the potential to reduce more complex defects and also to be used in future gravitational-wave detectors using conventional Gaussian beams.

DOI: 10.1103/PhysRevD.92.102002 PACS numbers: 04.80.Nn, 95.55.Ym, 95.75.Kk

I. INTRODUCTION

Gravitational wave (GW) detection is one of the principal challenges of the contemporary physics. GW are perturbations of the space-time metrics predicted by Einstein's general relativity [1], never directly detected up to now and produced by violent astrophysical phenomena or in the early phase of the Universe. Their detection has a huge scientific potential, as it would allow for not only a strong test of the theory, but also a new means of observing the Universe, both as an alternative and complement to electromagnetic waves [2].

Among the various efforts to detect GW, the second generation ground based interferometric detectors (Advanced Virgo [3], Advanced LIGO [4] and KAGRA [5]) will start soon to take data and they are likely to detect a first signal in the next five years [6].

These detectors are kilometric-scale Michelson interferometers with Fabry-Pérot cavities in the arms. The design sensitivity is limited by quantum noise and thermal noise above a few Hz. After the first detection, in order to enhance the science reach of this new field of gravitational-wave astronomy, several detector upgrades will be necessary and these are at varying degrees of development [7,8]. With regard to quantum noise, the main idea is to feed the output of the interferometer with a squeezed light source, a solution which is reaching a maturity phase [9–11]. No obvious solutions are present to obtain a substantial improvement of the thermal noise on the short-medium term. In order to directly reduce the source of the noise, material with lower mechanical losses and cryogenics techniques are under study or development. Both have technological issues. A detector with much longer arms has also been proposed in order to increase the sensitivity and bypass the difficulties related to the various upgrades [12].

Alternatively, rather than directly reducing the noise, it is possible to reduce the coupling between the laser beam and the thermal fluctuations by increasing the beam size, thus averaging the noise over a bigger surface. This can be done without increasing the size of the mirrors, by using beams with a larger profile, such as flat-top beams [13] or Laguerre-Gauss higher-order modes [14,15]. The latter have spherical wavefronts and then are compatible with standard spherical mirrors. Another idea to reduce the effect of the thermal noise is to use folded Fabry-Pérot cavities [16].

Over the past few years, several groups have studied the feasibility of a future GW interferometer illuminated by higher-order Laguerre-Gauss modes (LG) [17–24]. No fundamental obstacles have been found to the production of a high purity, high power and high efficiency $LG_{3,3}$ beam, or to the use of an $LG_{3,3}$ in a Fabry-Pérot Michelson interferometer. However, the degeneracy among modes of the same order is a serious limit of the application of this technique to future interferometric gravitational-wave detectors. When a $LG_{3,3}$ is injected in a high-finesse cavity, mirror figure errors can couple power within modes of the

*Corresponding author.
allocca@pi.infn.it

same order. These spurious modes generate a degradation of the cavity internal mode and thus, the cavity being part of a Michelson interferometer, a reduction of the visibility of the detector. Numerical simulations have shown that the state-of-the art polishing and coating techniques are unable to produce mirrors compatible with the requirements of interferometric gravitational-wave detectors. Even if some upgrades are expected, it is difficult to foresee what the mirror qualities will be in 5–10 years.

An alternative technique is to correct *in situ* the mirror figure errors by thermal compensation techniques. A heat source (coherent or incoherent) is sent to the mirror, after some suitable shaping [25,26]. This has the potential advantage of being more accurate and also bypasses the metrological limitation of coating/polishing techniques, using high sensitivity error signals coming directly from the interferometer.

In a previous publication [20] we have described the observation of the effects of the degeneracy in a Fabry-Pérot Michelson interferometer illuminated with an $LG_{3,3}$ mode and its comparison with the theory. Here we present the application of an incoherent radiation compensation technique on the tabletop interferometer and how the *in situ* compensation will increase the quality of one of the input cavity beams and the visibility of the interferometer.

The work is based on the experience of Virgo, where an incoherent source [27] was used to correct the radii of curvature of the mirrors, and on numerical simulations dedicated to the application of the *in situ* incoherent thermal compensation techniques to interferometry using higher-order Laguerre-Gauss interferometry [28,29]. Of course, the interest of this paper goes beyond the use of higher-order Laguerre-Gauss beams, since this *in situ* technique can potentially also be applied in a detector illuminated with a standard Gaussian beam, even if the influence of mirror defects is much smaller. Moreover, due to their enhanced sensitivity to mirror distortions, a higher-order LG mode can be also used as an auxiliary test beam to measure *in situ* mirror defects, even if the detector's main beam is the fundamental one.

The paper is organized in the following way: in Sec. II the Laguerre-Gauss modes are presented, as well as the problem of the degeneracy among modes of the same order. In Sec. III we describe the tabletop interferometer and its performance without thermal compensation. In Sec. IV we present the thermal compensation technique and its preliminary characterization. In Sec. V we present the results obtained and a comparison with a simulation. In Sec. VI we describe the conclusions and the prospects for this paper.

II. LG MODES AND DEGENERACY PROBLEM

The Laguerre-Gauss (LG) modes are a complete and orthogonal set of solutions for the paraxial wave equation [30,31]. A generic $LG_{p,l}$ mode is described by Eq. (1), where k is the wave number, $\Psi(z)$ is the Gouy phase, $L_p^{|l|}(x)$ is the generalized Laguerre polynomial, $w(z)$ and $R_c(z)$ are the size and radius of curvature of the beam at position z. Two indexes are used to define the Laguerre-Gauss modes: the radial index p and the azimuthal index l:

$$\psi_{p,l}(r,\phi,z) = \frac{1}{w(z)}\sqrt{\frac{2p!}{\pi(|l|+p)!}}\left(\frac{\sqrt{2}r}{w(z)}\right)^{|l|} \cdot L_p^{|l|}\left(\frac{2r^2}{w^2(z)}\right)\exp\left(i(2p+|l|+1)\Psi(z)\right) \cdot \exp\left(-\frac{kr^2}{2R_c(z)} - \frac{r^2}{w^2(z)} + il\phi\right). \quad (1)$$

Modes of the same order $2p+|l|$ have the same Gouy phase shift, they are therefore degenerate and can resonate simultaneously in a cavity. Distortions of the mirror surfaces, which deviate from a perfect spherical shape, induce a coupling between modes. Moreover, the degenerate modes will resonate in the cavity together with the injected one. Therefore, a non-negligible fraction of power will be transferred to degenerate modes leading to a significant degradation of the interferometer visibility, as underlined in [21–23].

As described in [22], it is possible to find a selection rule linking the input LG mode, the excited modes, and the Zernike polynomials describing the mirror defects. Zernike polynomials are a complete set of functions defined by the radial index n and the azimuthal index m, with $0 \le m \le n$. Mirror distortions described by the Zernike polynomial $Z_n^m(x,y)$ will couple power from the mode (p,l) into the mode (p',l') if

$$m = |l - l'|. \quad (2)$$

This relation, together with the request that the two LG modes are degenerate ($2p + l = 2p' + l'$), is very useful in associating the excited modes with mirror defects. Another way to understand mirror defects, used in [20], is to insert specific mirror defects into a numerical simulation of the interferometer, to reproduce the quality of the modes in various points of the interferometer and the amplitudes of the excited LG modes. In particular, an adimensional *intensity overlap integral* γ (already used in [17,19]) is used to estimate the quality of the modes in the considered points of the interferometer. It is defined as

$$\gamma = \frac{\iint I_{\text{meas}} \cdot I_{\text{theory}} dS}{\sqrt{\iint I_{\text{meas}}^2 dS} \cdot \sqrt{\iint I_{\text{theory}}^2 dS}}, \quad (3)$$

where $I_{\text{meas}} = |\psi_{\text{meas}}|^2$ is the transverse intensity distribution acquired by a beam profiler camera, $I_{\text{theory}} = |\psi_{\text{theory}}|^2$ is the theoretical intensity distribution, calculated from Eq. (1), and dS is the infinitesimal surface element.

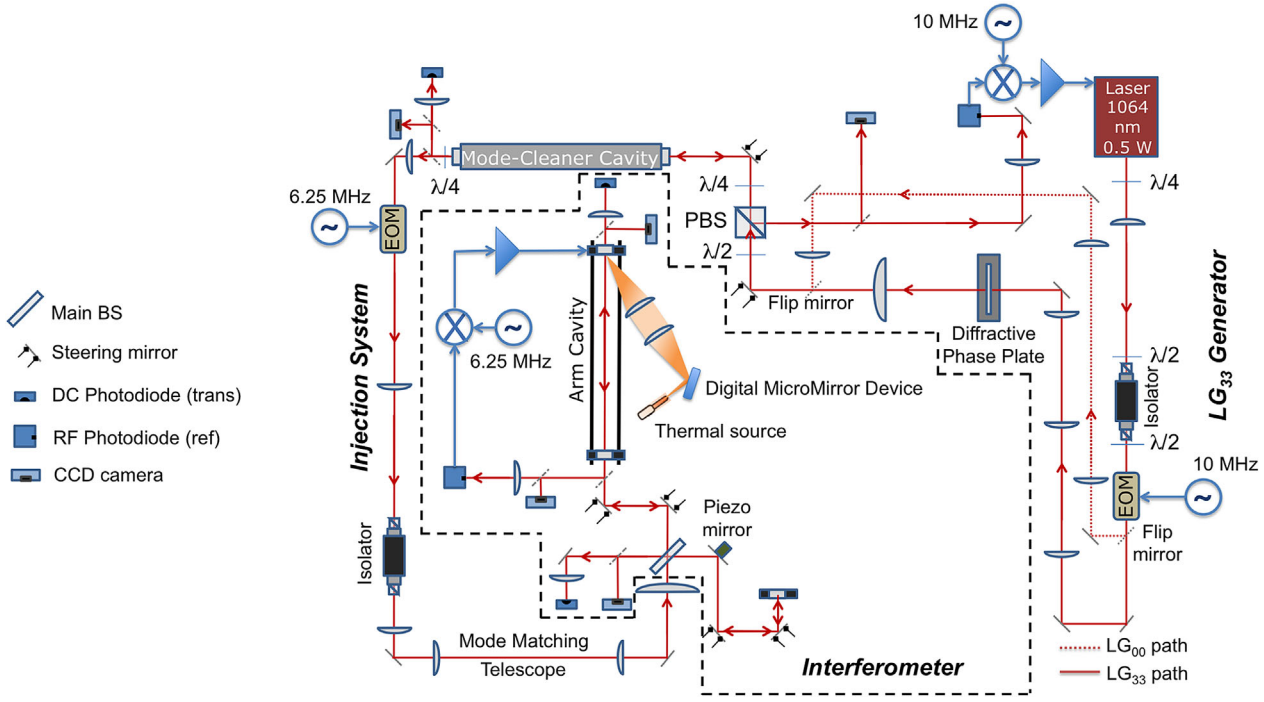

FIG. 1 (color online). Scheme of the experimental setup.

γ should be considered as an upper limit of the mode purity of the measured LG mode: indeed, the beam profiler camera acquires only the intensity, and in Eq. (3) the phase of the two modes is neglected.

III. THE $LG_{3,3}$ INTERFEROMETER

The scheme of the whole experimental setup is shown in Fig. 1. It consists of two main parts: the optical system, which is an asymmetric Fabry-Pérot Michelson interferometer illuminated by a $LG_{3,3}$ beam, and the thermal compensation system, which provides the heating pattern used to correct the mirrors defects. In this chapter we focus on the first part: the interferometer without thermal compensation.

A. Experimental setup

The optical setup can be divided in three main parts: the $LG_{3,3}$ generation system (*generator*), the optical elements used to inject the beam to the interferometer (*injection system*) and the asymmetric Fabry-Pérot Michelson interferometer itself (*interferometer*). Both the $LG_{3,3}$ and the Gaussian beam can be used in this setup. The alignment and the matching of the interferometer are done with the Gaussian beam.

The $LG_{3,3}$ generator and the injection system are the same as those used in [20]. The first part is mainly composed of a diffractive phase plate and a linear mode-cleaner cavity. The intensity distribution of the beam at the output of the mode-cleaner cavity is shown in Fig. 2(a). This is compared to the intensity distribution of a theoretical $LG_{3,3}$ beam, calculated using Eq. (1) for a beam at the same distance from the waist (set on the mode-cleaner input mirror) and shown in Fig. 2(b). The overlap integral, defined by Eq. (3), is higher than 99%. The second part consists of an electro-optic modulator (EOM), a Faraday isolator and a 4-lense mode matching telescope. The injection system is used to generate the 6.25-MHz radio-frequency sidebands for the lock of the arm cavity with a Pound-Drever-Hall scheme and to match the beam parameters with those of the Fabry-Pérot cavity. No degradation of the $LG_{3,3}$ beam due to the injection system is observed and the intensity overlap integral, at the input of the interferometer, is higher than 99%.

The last part of the optical setup is the asymmetric Fabry-Pérot Michelson interferometer. With respect to [20], one arm of the Michelson interferometer is a simple mirror instead of a Fabry-Pérot cavity. In this configuration an

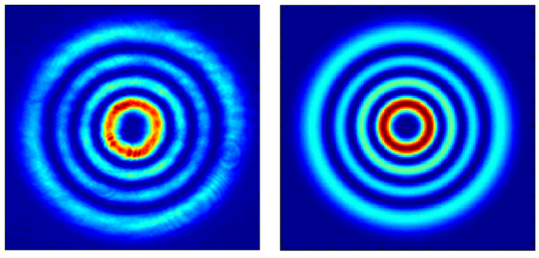

FIG. 2 (color online). Normalized intensity distribution recorded at the mode cleaner output (a) and theoretical $LG_{3,3}$ distribution at the same distance from waist (b).

almost perfect $LG_{3,3}$ beam, reflected by the mirror, interferes with a deformed $LG_{3,3}$ beam, reflected by the Fabry-Pérot cavity. In this way, the effect of the thermal compensation can be better isolated and studied. The length of the Fabry-Pérot cavity is 30 cm. It consists of a flat input mirror (ITM) and concave end mirror (ETM), characterized by a radius of curvature of 50 cm. The input mirror reflectivity is 97%, while that of the end mirror is 99.9%, which lead to a cavity finesse of 200. The BK7 linear expansion coefficient is about 10 times larger than that of the fused silica. Therefore, in order to enhance the effect of the thermal compensation, 1-inch diameter BK7 mirrors have been installed. Piezo actuators, used to control the cavity length, are installed on the end mirror mount. The spot size is 288 and 455 μm, respectively on the input and end mirrors. Photodetectors and CCD cameras are used to detect and acquire the beam reflected and transmitted from the cavity and the output beam of the interferometer. The photodiode used to detect the reflected beam from the cavity is also demodulated at 6.25 MHz in order to generate the error signal used to control the cavity length. A dithering technique is used to control the difference between the armlengths of the Michelson interferometer.

B. Interferometer performance without compensation

The interferometer was first operated without thermal compensation, in order to have a reference point, but also to identify the mirror defects responsible for the beam distortions and, therefore, the needed correction pattern.

The measured intensity distribution of transmitted and reflected beams is shown in Figs. 3(a) and 3(b), respectively. The intensity pattern recorded at the interferometer output when the cavity is at resonance and the Michelson is on the dark fringe is shown in Fig. 3(c). The fringe visibility of the interferometer is defined as

$$V = \frac{P_{\max} - P_{\min}}{P_{\max} + P_{\min}}, \tag{4}$$

where $P_{\max}$ and $P_{\min}$ are the maximum and minimum power levels measured at the interferometer output. Mainly

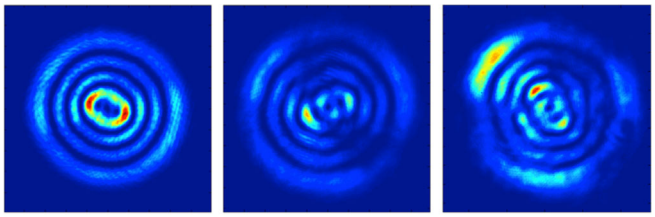

FIG. 3 (color online). $LG_{3,3}$ measured transverse intensity distributions at (a) cavity transmission, (b) reflection and (c) at the interferometer output when the cavity is at resonance and the Michelson is set on the dark fringe. The window side is 6 mm (same color scale for the three figures).

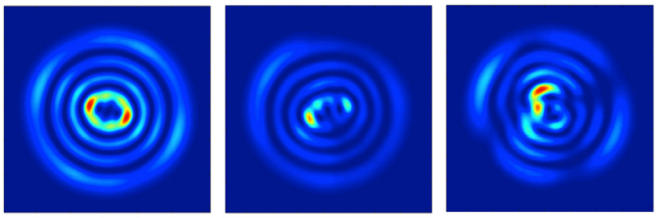

FIG. 4 (color online). $LG_{3,3}$ simulated transverse intensity distributions at (a) cavity transmission, (b) reflection and (c) at the interferometer output when the cavity is at resonance and the Michelson is set on the dark fringe. The window side is 6 mm (same color scale for the three figures).

because of the beam deformation produced by the degeneracy, the visibility measured without compensation is $V = 0.5$.

The characterization of the interferometer is done by analyzing the intensity pattern of transmitted and reflected beams. In particular, information about cavity mirror aberrations can be extracted from the intensity distribution of the transmitted beam, since it is relatively insensitive to cavity misalignments and mismatching, which instead strongly affect the reflected beam intensity distribution.

The analysis was undertaken in two ways. First, a numerical simulation with OSCAR [32,33] was performed, in the same manner as described in [20]. The cavity defects were tuned matching the measured and simulated shapes of the transmitted beam and their overlap integrals. The values of cavity misalignments and mismatching have been then tuned by using the reflected beam. Once the shapes and overlap integrals for the transmitted and reflected beams are matched [Figs. 4(a) and 4(b)], the dark fringe image and fringe visibility have been simulated without any further tuning of the simulation parameters [Fig. 4(c)]. Residual differences between simulated and experimental images are related to the misalignment of the second arm of the interferometer, which we are not considering for the moment. The simulated fringe visibility (49%) is consistent with the measured one (50%). The simulation parameters obtained are reported in Table I, while the simulated intensity distributions in transmission and reflection are shown in Figs. 4(a) and 4(b). Even if the cavity mirrors are different from [20] (fused silica in [20] and BK7 in this experiment), in order to reproduce the overlap integrals to $\sim 1\% - 2\%$ errors, it was, also in this case, only necessary to insert astigmatism.

TABLE I. Model parameters. ITM and ETM correspond to input and end mirrors of the Fabry-Pérot cavity, respectively.

Mismatching	Astigmatism		Misalignments	
Position error	Value	Angle	ITM	ETM
1.25 cm	13 nm PtV	22.5°	−15 μrad 29 μrad	13 μrad (x) 15 μrad (y)

In addition to the OSCAR simulation, in order to better determine the cavity mirror defects, in this experiment a decomposition of the measured transmitted beam intensity pattern as a function of the ten degenerate modes of order 9 was also performed. The decomposition is carried out as explained in [29]: first, the beam parameters, like beam center and size, are extracted from the experimental image. These parameters are used to compute the basis of 9th order modes $\Psi_i(x,y)$, $i=\{1,\ldots,10\}$. Finally, the transmitted power distribution is reconstructed as a linear combination of the basis elements as

$$P_{tr}(x,y;\alpha)=\left|\sum_{i=1}^{10}\alpha_i\Psi_i(x,y)\right|^2, \tag{5}$$

where the decomposition coefficients α_i are found by minimizing the difference between the experimental power image and the reconstructed one by using a gradient descent algorithm [34].

The coefficient amplitudes relative to the intensity distribution shown in Fig. 3(a) are reported in Fig. 5: the $LG_{3,3}$ mode couples mainly into modes $LG_{2,5}$ and $LG_{4,1}$. Using the selection rule of Eq. (2), we can therefore conclude that astigmatism (Z_2^2) is the principal mirror aberration in the cavity.

IV. THERMAL COMPENSATION SYSTEM

The thermal compensation system has to provide the proper heating pattern to correct the cavity defects. It is made up of a light source (*illumination system*) which generates a heating beam, an array of micromirrors, which defines the proper heating pattern (*correction map*) and is illuminated by the light source, and a *projection system*, which collects the light reflected by the micromirrors and images the correction map onto the mirror to compensate.

The illumination system consists of a heat source emitting incoherent broadband radiation with a Lambertian distribution. The chosen radiation source is a resistor, which filters out the high frequency current noise and is less affected by power instability. Here we employ a silicon-nitride heating element, the emissivity of which at temperatures of a thousand degree Celsius is around 0.93 for wavelengths greater than 2 μm, where the BK7 substrate absorption is high. In order to have an almost collimated heating beam, the source is installed in the focal point of a 1-inch diameter aluminum parabolic reflector.

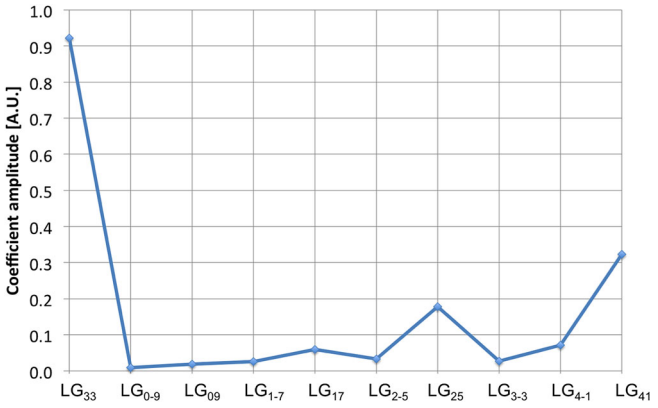

FIG. 5 (color online). Transmitted beam intensity decomposition in terms of the ten polynomials of 9th order.

The correction pattern is made by a DLP, a MEMS technology from Texas Instruments, which uses a digital micromirror device (DMD) [35]. It consists of an array of micromirrors 1 cm × 1.4 cm, organized in a two-dimensional matrix of 1024 columns by 768 rows, and is used to produce the suitable heating pattern needed to correct mirror defects. The power of this device lies in the fact that it allows, with the maximum flexibility, to project very complex heat patterns onto the mirror surface and, in principle, may be used in a feedback loop.

Finally, the projection system is used to image the heating pattern on the high-reflectivity surface of one of the two cavity mirrors. Its design has to fulfill some main requirements: collect all the power reflected by the micromirror array, have a high transmissivity for wavelengths higher than 2 μm and minimize the aberrations. At the same time it has to match the space needs of the existing setup. The selected projection system is a compromise for the above conditions. It consists of a two lens telescope made up of ZnSe and CaF_2 substrates, with an overall numerical aperture of 0.53.

A. Thermal compensation setup test

A first characterization of the thermal compensation setup was carried out separately from the interferometer. A simple pattern was projected on a BK7 mirror and the measured deformation was compared to the simulation predictions. In order to detect the mirror deformation, a probe Nd:YAG laser beam ($\lambda=1064$ nm) was used to image the mirror surface onto a wavefront beam analyzer through a telescope. The thermal compensation system was used to project a round spot with a 4.8 mm diameter onto the mirror. The induced deformation was predicted through a finite element simulation carried out with COMSOL MULTIPHYSICS [36].

In order to match experimental data with the simulation prediction, the parameter corresponding to the absorbed power was set to 8 mW. This value has been confirmed by a direct measurement of the power absorbed by the BK7 substrate. The matching between simulation and experimental data is shown in Fig. 6.

B. Estimation of the heat pattern needed for the compensation

Section III B showed that the main defect affecting the beam shape is astigmatism. In order to correct this, it is

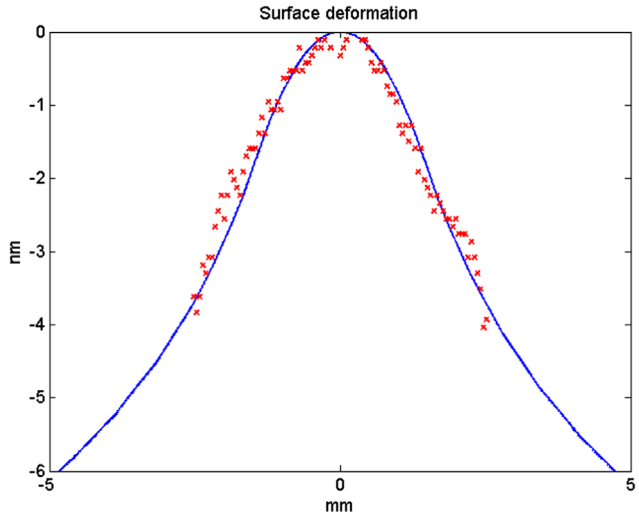

FIG. 6 (color online). Profile of mirror deformation induced by the projection of a round spot and 8 mW of absorbed power. Comparison between simulation (blue line) and experimental results (red stars).

necessary to find a heat pattern with a shape and size suitable to inducing the opposite deformation on the mirror.

The heat pattern size on the mirror depends on the region of the mirror "seen" by the laser YAG beam. Since the Gaussian radius of the beam on the ETM is 455 μm, this gives an effective diameter of the $LG_{3,3}$ mode of 4 mm, outside which the power is only a few ppm. In order to have some margin, a heat pattern of 6 mm size was chosen.

A finite element simulation carried out with COMSOL MULTIPHYSICS [36] demonstrated that the compensation can be obtained by projecting two circles onto the mirror, as shown in Fig. 7(a). Taking into account the maximum intensity that the compensation system is able to provide in this configuration, the simulation predicts an astigmatic deformation with a PtV amplitude of 8 nm, as shown in Fig. 7(b), which is about one half of the total astigmatism needed to be corrected.

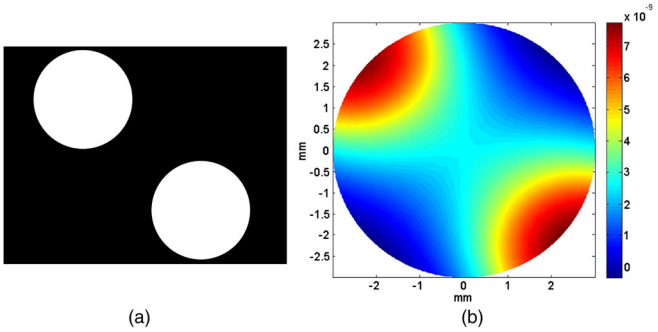

FIG. 7 (color online). (a) Pattern imaged on the mirror and used as an absorption map in the COMSOL simulation. (b) Simulated mirror deformation obtained with heat pattern (a) for an absorbed intensity of 550 W/m^2. The color bar is in meters.

V. THERMAL COMPENSATION RESULTS

In this section we describe the performance of the $LG_{3,3}$ interferometer in the presence of the thermal compensation system. In particular, the thermal compensation has been effective at reducing and enhancing astigmatism of the ETM by projecting the pattern shown in Fig. 7(a) and the same pattern rotated by 90°, respectively. The reference configuration is the one already presented and analyzed in Sec. III.

The transverse intensity distributions of the beam transmitted by the Fabry-Pérot cavity in the three configurations are shown in Fig. 8(a). The effect of the thermal correction is clearly visible from the change of the beam ellipticity.

The intensity distributions for the Fabry-Pérot cavity reflected beams in the three configurations are shown in Fig. 9(a). The asymmetry of the distributions is due to the presence of residual misalignments.

Finally, the intensity patterns at the interferometer output when the cavity is at resonance and the Michelson is set on the dark fringe for the three configurations are shown in Fig. 10(a). A reduction of the power at the dark port is evident for the lower astigmatism configuration. The effect of the correction is evident also in terms of fringe visibility: 35% when astigmatism is increased and 62.5% when it is reduced, compared to the 50% in absence of compensation.

Table II summarizes the obtained results in terms of overlap integrals (O.I.), power transmitted by the single Fabry-Pérot cavity and fringe visibility for the three configurations.

The OSCAR simulation described in Sec. III B was also used to reproduce the experimental results. The simulation parameters obtained are reported in Table III and they demonstrate that we are able to induce an astigmatic deformation of about 7 nm PtV. This value is compatible with the first estimation reported in Sec. IV B, which was of

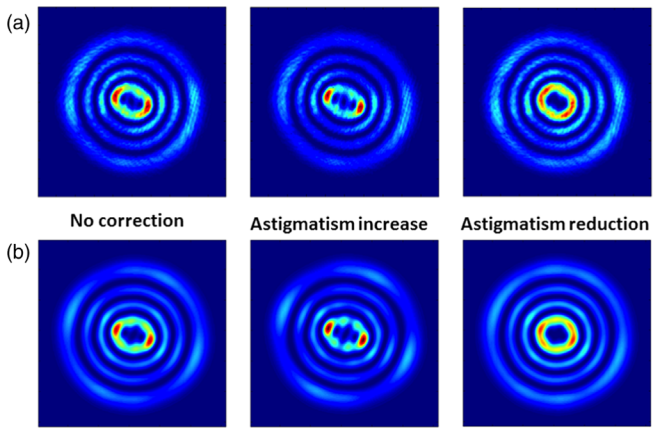

FIG. 8 (color online). $LG_{3,3}$ transverse intensity distributions measured (a) and simulated (b) at cavity transmission. Left column: reference condition (presented in Sec. III). Central column: astigmatism enhancement. Right column: astigmatism reduction. The color scale is the same for the three configurations.

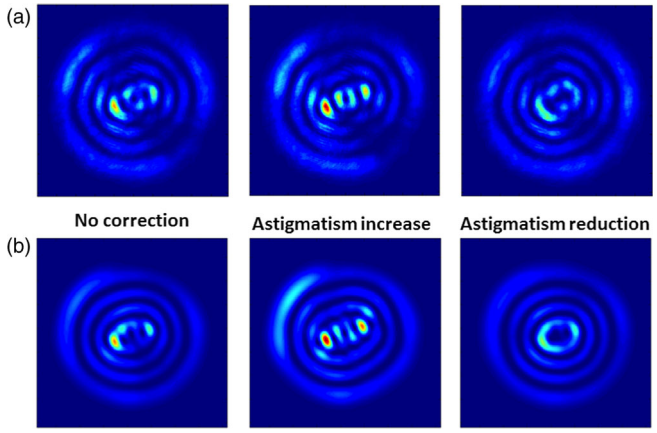

FIG. 9 (color online). $LG_{3,3}$ transverse intensity distributions measured (a) and simulated (b) at cavity reflection. Left column: reference condition (presented in Sec. III). Central column: astigmatism enhancement. Right column: astigmatism reduction. The color scale is the same for the three configurations.

about 8 nm PtV. Moreover, the corresponding simulated overlap integrals, powers transmitted by the Fabry-Pérot cavity and fringe visibilities are reported in Table IV. The simulated intensity distributions in transmission and reflection are shown in Figs. 8(b) and 9(b), while the dark fringe images are shown in Fig. 10(b). The simulated images and the interferometer performance are in good agreement with respect to those measured.

To describe the effect of the compensation in terms of scattering into degenerate modes, the beam decomposition analysis was applied to all of the transmitted beam intensity images of Fig. 8(a), and is reported in Fig. 11. The thermal correction of astigmatism reduces the scattering into modes $LG_{2,5}$ and $LG_{4,1}$ while more power is coupled in the $LG_{3,3}$

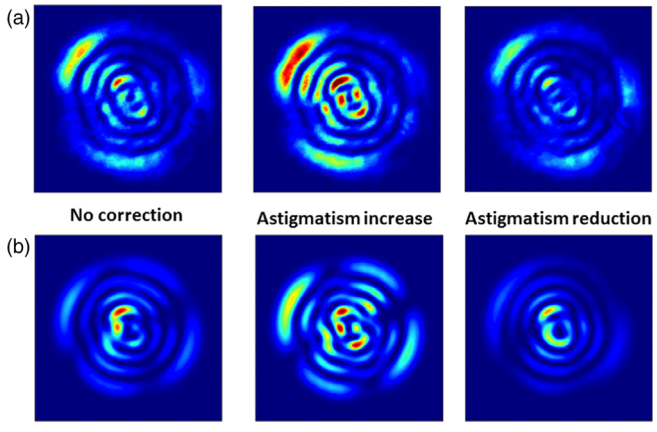

FIG. 10 (color online). $LG_{3,3}$ transverse intensity distributions measured (a) and simulated (b) at the interferometer output when the cavity is at resonance and the Michelson is set on the dark fringe. Left column: reference condition (presented in Sec. III). Central column: astigmatism enhancement. Right column: astigmatism reduction. The color scale is the same for the three configurations.

TABLE II. Interferometer performance without and with the thermal compensation system.

	No compensation	Astigmatism enhancement	Astigmatism reduction
O.I. (TX)	93.8%	89%	97.3%
O.I. (Ref)	77.7%	68.1%	86.4%
Power (TX)	100%	91%	109%
Visibility	50%	35%	62.5%

TABLE III. Model parameters.

Astigmatism enhancement configuration				
Mismatching	Astigmatism		Misalignments	
Position error	Value	Angle	ITM	ETM
1.25 cm	20 nm PtV	22.5°	−15 μrad 29 μrad	25 μrad (x) −22 μrad (y)
Astigmatism reduction configuration				
Mismatching	Astigmatism		Misalignments	
Position error	Value	Angle	ITM	ETM
1.25 cm	7 nm PtV	22.5°	−15 μrad 29 μrad	−29 μrad (x) 9 μrad (y)

TABLE IV. Simulated interferometer performances with thermal compensation system.

	No compensation	Astigmatism enhancement	Astigmatism reduction
O.I. (TX)	94.8%	90.6%	98.1%
O.I. (Ref)	77.7%	71.7%	86%
Power (TX)	100%	92%	110%
Visibility	49%	32%	65%

mode. On the other hand, the opposite situation is found when astigmatism is increased: couplings into modes $LG_{2,5}$ and $LG_{4,1}$ are enhanced, and less power is found in the $LG_{3,3}$ mode.

Both the numerical simulation and the mode decomposition analysis demonstrate that the effect of the thermal compensation is well understood, as is the reduction of the negative effects of high-order LG mode degeneracy within the interferometer.

A. Discussion

An astigmatism modification of $\sim \pm 50\%$ has been obtained with this thermal compensation system. This compensation level corresponds to the maximum power delivered by our particular thermal source. The use of a more powerful thermal source should in principle allow a better compensation. In order to provide an estimate of the

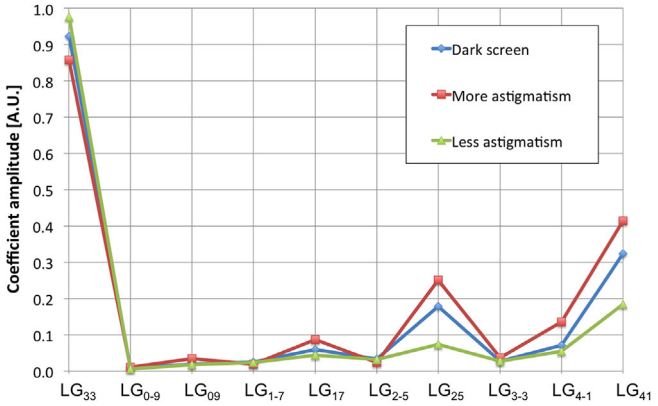

FIG. 11 (color online). Transmitted beam decomposition in modes of order 9. The astigmatism thermal correction reduces the scattering of $LG_{3,3}$ into modes $LG_{2,5}$ and $LG_{4,1}$ while more power is coupled in the $LG_{3,3}$ mode. On the other hand, couplings into modes $LG_{2,5}$ and $LG_{4,1}$ are enhanced when mirror astigmatism is increased, and less power is found in the $LG_{3,3}$ mode.

power needed for a complete astigmatism correction, we have plotted the change of the beam modes composition as a function of the power dissipated by heat source. In particular, the change can be noticed in the amplitude of the coefficient relative to the $LG_{4,1}$ mode, as shown in Fig. 12. The linear fit of Fig. 12 suggests that the coefficient amplitude could be reduced to zero with a power approximately twice as great as that available with our setup.

It is also important to remark that a careful alignment and focus procedure of the heating source on the mirror is needed to obtain good compensation performance. When applied, this procedure allows to identify the beam astigmatism axes, avoiding a rotation of the astigmatism during compensation.

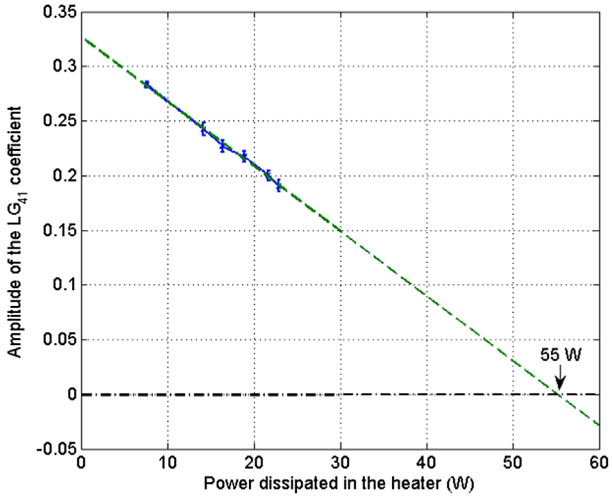

FIG. 12 (color online). Amplitude of the coefficients relative to the mode $LG_{4,1}$ while varying the heating power. A linear fit shows that having about twice the power from the compensation system allows to completely correct astigmatism.

A slight change of end mirror alignment is noticed among the three considered configurations. This effect may be due to the thermal pattern distortion due to a non-orthogonal incidence, or to a very small miscentering of the heat pattern with respect to the cavity beam.

Moreover, it must be noticed that not all of the potentialities of the DMD have been exploited: indeed, the compensation pattern imaged on the mirror had a very simple shape. However, the obtained results allowed us to prove the working principle and, improving the system design, it will be possible to have more power and perform more detailed corrections. For example, using the transmitted or reflected beam images as an error signal to compute the surface correction map, as explained in [29], it is in principle possible to increase the $LG_{3,3}$ mode purity inside the cavity, and the change of the projection map in a loop can be achieved very quickly and easily thanks to the DMD.

VI. CONCLUSIONS AND FUTURE STEPS

We have shown how an *in situ* thermal compensation technique using an incoherent source and a shaping system based on a micromirrors device can reduce the astigmatism of a mirror used inside a Fabry-Pérot cavity, illuminated with a $LG_{3,3}$ mode. Due to the compensation, the quality of the internal beam increases in agreement with the theory. When the cavity is inserted in an asymmetric Fabry-Pérot Michelson interferometer, it is possible to increase the contrast of the interferometer. Even if preliminary, these results shows how the *in situ* techniques can release the constraints imposed by the use of higher-order Laguerre-Gauss modes in future interferometric gravitational-wave detectors. Moreover, this particular scheme using a system of digitally controlled micromirrors has the potential to reduce more complex defects, projecting more complex patterns and also to be used in a feedback system, using the beam images as error signals.

ACKNOWLEDGMENTS

The authors would like to thank the Laboratoire d'Annecy-le-Vieux de Physique des Particules for the support with the digital control system and photodiode readout; H. Halloin and P. Prat for discussions and support with the analog electronics. M. Granata and R. Ward have contributed to the realization of the $LG_{3,3}$ generator described in [17], and F. Kéfélian has contributed at the realization of the $LG_{3,3}$ interferometer described in [20]. G. V. would like to acknowledge the support of the National Science Foundation and the LIGO Laboratory. LIGO was constructed by the California Institute of Technology and Massachusetts Institute of Technology with funding from the National Science Foundation, and operates under Cooperative Agreement No. PHY-0757058. Advanced LIGO was built under Award No. PHY-0823459.

Finally, we would like to thank Adam Kutynia and Nicolas Smith-Lefebvre for their help in setting up the DMD board, Gary Hamming for the reading of the manuscript, and Eric Genin, Antonino Chiummo and Paul Fulda for useful discussions. This work is supported by the Agence Nationale de la Recherche under Grant No. 2010-BLANC-0416-01. M. T. is supported by the European Gravitational Observatory.

[1] C. W. Misner, K. S. Thorne, and J. A. Wheeler, *Gravitation* (W.H. Freeman and Company, San Francisco, 1973).
[2] B. S. Sathiaprakash and B. F. Shutz, Living Rev. Relativity **12**, 2 (2009).
[3] F. Acernese *et al.* (Virgo Collaboration), Classical Quantum Gravity **32**, 024001 (2015).
[4] J. Aasi *et al.* (LIGO Scientific Collaboration), Classical Quantum Gravity **32**, 074001 (2015).
[5] Y. Aso, Y. Michimura, K. Somiya, M. Ando, O. Miyakawa, T. Sekiguchi, D. Tatsumi, and H. Yamamoto (Kagra Collaboration), Phys. Rev. D **88**, 043007 (2013).
[6] J. Abadie *et al.*, Classical Quantum Gravity **27**, 173001 (2010).
[7] M. Abernathy *et al.*, http://www.et-gw.eu/etdsdocument.
[8] J. Miller, L. Barsotti, S. Vitale, P. Fritschel, M. Evans, and D. Sigg, Phys. Rev. D **91**, 062005 (2015).
[9] M. Evans, L. Barsotti, P. Kwee, J. Harms, and H. Miao, Phys. Rev. D **88**, 022002 (2013).
[10] H. Grote, K. Danzmann, K. L. Dooley, R. Schnabel, J. Slutsky, and H. Vahlbruch, Phys. Rev. Lett. **110**, 181101 (2013).
[11] J. Aasi *et al.*, Nat. Photonics **7**, 613 (2013).
[12] S. Dwyer, D. Sigg, S. W. Ballmer, L. Barsotti, N. Mavalvala, and M. Evans, Phys. Rev. D **91**, 082001 (2015).
[13] E. D'Ambrosio, Phys. Rev. D **67**, 102004 (2003).
[14] B. Mours, E. Tournefier, and J.-Y. Vinet, Classical Quantum Gravity **23**, 5777 (2006).
[15] J.-Y. Vinet, Living Rev. Relativity **12**, 5 (2009).
[16] S. W. Ballmer and D. J. Ottaway, Phys. Rev. D **88**, 062004 (2013).
[17] M. Granata, C. Buy, R. Ward, and M. Barsuglia, Phys. Rev. Lett. **105**, 231102 (2010).
[18] P. Fulda, K. Kokeyama, S. Chelkowski, and A. Freise, Phys. Rev. D **82**, 012002 (2010).
[19] L. Carbone, C. Bogan, P. Fulda, A. Freise, and B. Willke, Phys. Rev. Lett. **110**, 251101 (2013).
[20] A. Gatto, M. Tacca, F. Kéfélian, C. Buy, and M. Barsuglia, Phys. Rev. D **90**, 122011 (2014).
[21] T. Hong, J. Miller, H. Yamamoto, Y. Chen, and R. Adhikari, Phys. Rev. D **84**, 102001 (2011).
[22] C. Bond, P. Fulda, L. Carbone, K. Kokeyama, and A. Freise, Phys. Rev. D **84**, 102002 (2011).
[23] M. Galimberti *et al.*, Einstein Telescope internal document, https://tds.ego-gw.it/.
[24] B. Sorazu *et al.*, Classical Quantum Gravity **30**, 035004 (2013).
[25] R. C. Lawrence, Ph.D. thesis, MIT [Report No. LIGO-P030001-00-R, 2003].
[26] S. Ballmer, Ph.D. thesis, MIT [Report No. LIGO-P060043-00-Z, 2006].
[27] T. Accadia *et al.*, Classical Quantum Gravity **30**, 055017 (2013).
[28] R. A. Day, G. Vajente, M. Kasprzack, and J. Marque, Phys. Rev. D **87**, 082003 (2013).
[29] G. Vajente and R. A. Day, Phys. Rev. D **87**, 122005 (2013).
[30] A. E. Siegman, *Lasers* (University Science Books, Sausalito, California, 1986).
[31] H. Kogelnik and T. Li, Appl. Opt. **5**, 1550 (1966).
[32] J. Degallaix, J. Phys. Conf. Ser. **228**, 012021 (2010).
[33] http://www.mathworks.fr/matlabcentral/fileexchange/20607-oscar.
[34] W. H. Press *et al.*, *Numerical Recipes: The Art of Scientific Computing*, 3rd ed. (Cambridge University Press, Cambridge, England, 2007).
[35] http://www.ti.com/lsds/ti/analog/dlp/overview.page.
[36] https://www.comsol.com/comsol-multiphysics.